AIAA JOURNAL
Vol. 38, No. 9, September 2000

Coherent Anti-Stokes Raman Scattering Measurements and Computational Modeling of Nonequilibrium Flow

F. Grisch,* P. Bouchardy,† V. Joly,‡ and C. Marmignon§
ONERA, 92322 Châtillon Cedex, France
and
U. Koch¶ and A. Gülhan¶
DLR, German Aerospace Research Center, 5000 Cologne, Germany

An experimental study is conducted in a high-enthalpy continuous facility to investigate the nonequilibrium shock-layer airflow induced by a two-dimensional body. The rotational and vibrational temperatures of nitrogen as well as the number density are measured by recording the rovibrational spectra of molecular nitrogen using coherent anti-Stokes Raman scattering spectroscopy. Measurements are performed in the freestream and within the shock layer induced by a disk model. Difficulties specific to the application of an optical technique to a high enthalpy flow are discussed, and flows parameters are given. The nozzle and shock-layer flows are modeled numerically using a nonequilibrium Navier–Stokes solver. Good agreement is achieved between the experimental and calculated results.

I. Introduction

THE various physical and chemical phenomena that take place in hypervelocity flowfields during the reentry phase of aerospace flight are extremely important for the design of the next generation of reuseable spacecraft. Improving our understanding of these complex phenomena is being achieved through combined developments of computational fluid dynamics (CFD) and experiments in hypersonic facilities.

Within this framework, arc-heater wind tunnels are useful for simulation of hypersonic flow conditions for measurements on realistic models that will be extrapolated to flight conditions. These tools are also of great interest for code validation purposes. However, the aerothermodynamic states of the flows produced in them are not yet well understood. This is due to the complexity of the physical and chemical phenomena occurring in these flows. The flow undergoes vibrational excitation, dissociation, and ionization. Because of the relatively low-density environment produced in these facilities, the flow is generally in nonequilibrium in both chemical composition and internal modes. Although real flight conditions cannot be reproduced, a significant prediction of the thermal and chemical states of the flow upstream of the model, along with its nonequilibrium calculation, will allow comparison of experiments and numerical results around the model.

Experimentally, laser diagnostics based on molecular scattering have received considerable attention for application in hypersonic test facilities thanks to their nonintrusive nature and their properties, among which are excellent temporal and spatial resolutions. These methods can provide information directly related to the parameters of the molecular state of the gas including temperature, density, and velocity. Among these techniques, Raman scattering, electron beam fluorescence, and laser-induced fluorescence (LIF) seem promising in low-density and high-temperature hypersonic flows.[1–5] In particular, coherent anti-Stokes Raman scattering (CARS) belongs to these techniques. Both local number densities and temperatures can be determined from the CARS signal. The density is related to the absolute intensities of the spectral features whereas temperatures can be inferred from the relative intensities of rotational and vibrational lines contributing to the CARS spectrum. Determining these physical qualities simultaneously would then be extremely useful in high enthalpy flows.

The objective of the present work is to study the behavior of a nonequilibrium hypersonic airflow interacting with a shock wave surrounding a model. The experiment completes previous efforts already done using planar LIF on NO (Ref. 6). Scanning CARS,[7] well adapted to the study of low-pressure continuous flows, is used to probe N_2 in a nonequilibrium hypersonic airflow produced in the arc-heater wind tunnel. This arc-jet facility is commonly used for the investigation of heat protection material in spacecraft reentry conditions with relevant chemistry. From the data, rotational and vibrational temperatures of N_2 and number densities have been deduced in the freestream and behind a shock wave surrounding a blunt body placed in the flow. The results are used as a database to validate the Navier–Stokes solver CELHYO developed at ONERA for prediction of viscous flows in chemical and thermal nonequilibrium.[8]

II. Theoretical Considerations

A. CARS

The theory of CARS has been described in detail elsewhere.[9] CARS is a nonlinear optical technique that may be used to measure the rotational and vibrational population distributions of any molecule having a Raman active transition. From such distributions, one then deduces the number density of the species under study and its rotational and vibrational temperatures if the distributions are Boltzmann like. CARS is observed when three waves of frequencies, ω_0, ω_1, and ω_2, pass through a gas mixture. If the frequency difference $(\omega_1 - \omega_2)$ is close to the Raman-active vibrational frequency ω_P, an intense beam with frequency $\omega_3 = \omega_0 + (\omega_1 - \omega_2)$ will be generated in the forward direction of the incident waves. The two coherent incident waves ω_1 and ω_2 force the molecules to oscillate in phase at the frequency $(\omega_1 - \omega_2)$. Then the ω_0 radiation is scattered off by molecules whose polarizability is modulated by the oscillation. The new coherent wave is created through the third-order nonlinear susceptibility $\chi^{(3)}$. Usually, the same wave is used to pump and probe the molecular oscillation $(\omega_0 = \omega_1)$ and the anti-Stokes frequency is then given by $\omega_3 = \omega_1 + (\omega_1 - \omega_2)$.

Received 7 December 1998; revision received 7 February 2000; accepted for publication 16 February 2000.

*Research Scientist, Département Mesures Physiques, 29, avenue de la division Leclerc, BP 72.
†Research Engineer, Département Mesures Physiques, 29, avenue de la division Leclerc, BP 72.
‡Research Scientist, Département Optique Théorique et Appliquée, 29, avenue de la division Leclerc, BP 72.
§Research Scientist, Département Aérodynamique Fondamentale et Expérimentale, 29, avenue de la division Leclerc, BP 72.
¶Research Scientist, Institute of Fluid Mechanics, Postfach 906058.

As is customary in CARS, information about the state of the molecular system is derived from line shapes and line intensities. Spectra are recorded as a function of the frequency difference $(\omega_1 - \omega_2)$, and the CARS signal intensity is proportional to the square of the nonlinear susceptibility $\chi^{(3)}$, the resonances of the latter having an amplitude proportional to quantum state population differences.[9] When the pump beam ω_1 is monochromatic, the CARS intensity $I(\omega_1 - \omega_2)$ for an isolated line at ω_{vJ} is then given by[10]

$$I(\omega_1 - \omega_2) = K\left\{\Delta N_{vJ}\left(\frac{d\sigma}{d\Omega}\right)_{vJ}\right\}^2 S(\omega_1 - \omega_2) P_1^2 P_2 \left\{\int_{\Gamma_{\omega_2}} L(\omega_2)\, d\omega_2 \times \left|\int \frac{g(v_z)\, dv_z}{(\omega_1 - \omega_2) - \omega_{vJ}(1 - v_z/c) - i\Gamma_c} + \chi_{nr}\right|^2\right\} \quad (1)$$

In this expression, P_1 and P_2 are the pump and the Stokes laser powers, respectively. ΔN_{vJ} is the population difference between the initial and the final states of the Raman transition and $d\sigma/d\Omega$ is the spontaneous Raman cross section. K is a proportionality factor that take into account the optical transmission of the signal channel, the detector efficiency, and the probe volume geometry. The expression inside the braces represents the line profile. It is the convolution of the Stokes laser profile $L(\omega_2)$ with the Raman line profile. The Doppler broadening is taken into account by the term $\omega_{vJ} v_z/c$, where v_z is the projection of the velocity along the difference of wave vectors $(\boldsymbol{K}_1 - \boldsymbol{K}_2)$ of the pump and Stokes waves and $g(v_z)$ is the Maxwell–Boltzmann distribution function. Γ_c is the collisional linewidth (half-width at half-maximum). Here χ_{nr} is a slowly varying nonresonant term; it is a background contribution due to electrons and remote resonances from the other species present. For all spectra reported, χ_{nr} was found to be negligible and was systematically neglected. $S(\omega_1 - \omega_2)$ represents the effects of saturation due to the Raman pumping and the Stark effect.[11] It describes the deviation of the CARS signal strength vs pump powers from the classical $P_1^2 P_2$ dependence. Without saturation effects, $S(\omega_1 - \omega_2) = 1$. In the saturation regime, this value depends on many parameters, and a resolution of the time evolution of the density matrix equation for each velocity group is necessary.[12]

The spontaneous cross section, up to a constant factor, is

$$\frac{d\sigma}{d\Omega} = \left[\alpha^2 + \frac{4}{45}\gamma^2 \frac{J(J+1)}{(2J-1)(2J+3)}\right](v+1) \quad (2)$$

for the Q branch of the stretching mode. The lower state has rotational and vibrational quantum numbers J and v, respectively. Also, α and γ are the mean molecular polarizability and anisotropy, respectively.

For a nonequilibrium flow, the population fractions in Eq. (1) can be written as

$$N_{vJ} = g_J \frac{N(2J+1)\exp[-G(v)/kT_{vib}]\exp[-F_v(J)/kT_{rot}]}{Q_{vib}Q_{rot}} \quad (3)$$

where the vibrational temperature T_{vib} is allowed to be different from the rotational temperature T_{rot}. $G(v)$ and $F_v(J)$ are the vibrational and rotational term values.[13] The nuclear spin multiplicity g_J differs from unity for molecules with ortho- and paraspecies such as nitrogen. These species are assumed not to interconvert during the expansion, so that the rotational partition function Q_{rot} is calculated by summing over only even (or odd) J values for a given spin species. Q_{vib} is the vibrational partition function.

Because of the low-density nature of the expanding flow, scanning CARS has been chosen to record the rotational and vibrational populations of molecular species to ensure the best instrumental sensitivity. It uses a monochromatic laser for the pump beam and a tunable narrowband laser for the Stokes beam. The total intensity $I(\omega_1 - \omega_2)$ is recorded as a function of the frequency difference $(\omega_1 - \omega_2)$ by step by step scanning the Stokes frequency while the pump frequency is fixed. At the same time, a second CARS signal $R(\omega_1 - \omega_2)$ is generated in a reference channel identical to the main detection channel. The latter is generally used to monitor signal fluctuations resulting from laser power instabilities and from changes in dye efficiency vs wavelength.[9]

B. Data Handling

According to Eqs. (1–3), the area under each Q rotational line, with the quantity $\{I(\omega_1 - \omega_2)/R(\omega_1 - \omega_2)\}^{1/2}$, is calculated by integrating the line profile and divided by the reference signal. This result is proportional to the rotational population difference and, thus, to the rotational population if one assumes a nondependence of the rotational temperature with the vibrational band. The rotational temperature T_{rot} of a given vibrational transition (v'' and v') is measured by plotting a Boltzmann diagram of the rotational line amplitudes vs the rotational energies $F_{v''}(J)$. T_{rot} is obtained from a linear regression with an accuracy ΔT_{rot} depending on the number of rotational lines, the energy gap between the lower and the upper energy levels probed, the signal-to-noise ratio at peak intensity of each rotational line, and the value of T_{rot}. A simple calculation shows that ΔT_{rot} is proportional to T_{rot}^2 for fixed conditions. As a consequence, ΔT_{rot} ranges generally from 10 to 50 K for low v and increases quickly for high v when the signal strength decreases. Detailed expressions of the data processing may be found in a previous paper.[7]

The total population difference between the v and $v+1$ vibrational states are deduced assuming a Boltzmann distribution at T_{rot} on the entire vibrational bands. Each vibrational band strength is corrected for its dependence on v contained in the Raman cross section and in the line profile through the Doppler broadening. The vibration temperature T_{vib}, if existing, is deduced from the ratio of the vibrational population of two vibrational states. Summing the vibrational populations gives the total number density of the species using a scaling factor obtained from a calibration experiment in which temperature, pressure, and composition are known.

C. CFD Calculations

The Navier–Stokes solver CELHYO,[8] modeling internal or external (one- or two-dimensional) hypersonic viscous flows in chemical and thermal nonequilibrium, was developed at ONERA. It has been used here to simulate the high enthalpy flow in the nozzle and the flow around the model.

The CELHYO code treats ideal mixtures of perfect gases made of n_h heavy species, with n_m of them being molecular species. The mixture is assumed to be composed of the five neutral species N_2, O_2, NO, N, and O. All of the species are described with the same mean velocity v. Three degrees of freedom are considered: the translation and the rotation, described by one temperature T_{trans}; the vibration; and the dissociation. Energy is supposed to follow a Boltzmann distribution. The N_2 and O_2 vibrational energy are characterized by two distinct vibrational temperatures T_v. For the NO molecule, previous determinations[14,15] of the vibrational relaxation time give characteristic times two orders of magnitude less than that of O_2 between 3000 and 7000 K. On the basis of these results, the NO molecule should then be considered at equilibrium (as in most CFD calculations). However, recent measurements of rotational and vibrational temperatures in an expanding flow shows nonequilibrium.[16] In the following, consider that the NO mass fraction is about 5% all along the nozzle, which is small, the vibrational and the translational temperatures of NO are assumed to be equal.

The second-order diffusive convective system governing the mixture under consideration is

$$\partial_t \boldsymbol{u} + \operatorname{div}[\boldsymbol{f}(\boldsymbol{u}) - \boldsymbol{D}(\boldsymbol{u}) \operatorname{grad} \boldsymbol{u}] = \Omega \quad (4)$$

where $\boldsymbol{f}$ is the inviscid fluxes. Dissipative phenomena are modeled by the diffusive tensor $\boldsymbol{D}$. The source term Ω represents the presence of nonequilibrium phenomena. The variable $\boldsymbol{u}$ is

$$\boldsymbol{u}^T = \left[(\rho_\alpha)_{1 \le \alpha \le n_h}, \rho v_1, \rho v_2, \rho E, (\rho_\beta e_{v;\beta})_{1 \le \beta \le n_v}\right] \quad (5)$$

where E is the total energy of the mixture, $\boldsymbol{v} = (v_1, v_2)$ is the mean velocity, and $e_{v;\beta}$ is the vibrational energy of the molecular species β assumed to be in thermal nonequilibrium. The mixture pressure p is defined by

$$p = \kappa_{\mathrm{tr}} \left\{ \rho E - \frac{1}{2}\rho v^2 - \sum_{\beta} \rho_\beta e_{v;\beta} - \sum_{\alpha} \rho_\alpha \left[h_\alpha^0 + e_\alpha(T) \right] \right\} \quad (6)$$

where $\kappa_{\mathrm{tr}} = \gamma_{\mathrm{tr}} - 1$ and e_α and h_α^0 are the translation and the heat of formation of species α, respectively.

Detailed expressions of source terms and of the diffusive tensor may be found in a previous paper.[8] The chemical reaction model taken for air is Gardiner's.[17] It consists of 15 dissociation reactions and two exchange reactions. The vibrational relaxation of diatomic species (N_2 and O_2 for air) occurs through vibrational–translational transfers, which are modeled following the Landau–Teller rule[18] and using the molecular collisional data[19] for N_2, O_2, and NO and the atomic collisional data[20] for N and O. Vibrational–vibrational processes are also taken into account with the formulation for the source term and the data.[20]

The CELHYO code solves the Navier–Stokes balance equations on curvilinear structured meshes using a fully implicit, finite volume method. The viscous part is discretized according to a central differencing procedure, whereas a quasi-second-order accurate upwind scheme yields an approximation for the inviscid operator. Upstreaming is achieved using an approach for upwind bias referred to as hybrid upwind splitting.[21] The method is designed to combine the natural strengths of the Oscher solver and the Van Leer splitting to improve accuracy in the resolution of boundary layers and robustness in the capture of nonlinear waves, respectively. Note that no switch to be tuned up is involved here. Second-order accuracy is achieved using a MUSCL approach written in primitive variables. Special attention is paid when the method is applied to mass fractions to preserve the local numbers of elements.

The implicit operator is made of a linearization of both the inviscid and viscous fluxes in addition to all of the source term Jacobian matrices. For a detailed presentation of this time-marching algorithm, the reader is referred to Ref. 8.

A no-slip velocity condition together with a constant temperature T_w for the translational and vibrational modes are prescribed for the wall boundary. The wall is assumed to be noncatalytic, and the normal gradient of pressure at the wall is zero.

III. Experimental Setup

A. Arc-Heater Wind Tunnel

The facility is the arc-heated wind-tunnel L2K of DLR Cologne used primarily for testing the thermal protection materials developed for spacecraft under high enthalpy flow conditions.[22] L2K is designed to run continuously for several hours, and it offers a wide choice of operating conditions typical of those encountered at the stagnation point during a Shuttle reentry. The main parts of the facility are the arc heater and the power supply, the test chamber with the expansion nozzle, the freejet and diffuser, the heat exchanger, and the supply equipment. The power-supply system is based on a thyristor-controlled rectifier consisting of four units of 350 kW (600 A, 590 V), which can be switched alternatively to a parallel or series connection. The current is controlled during the test while the effective voltage depends on the resistance of the arc heater. An arc heater of the hollow-electrode concept (Huels type) has been applied for the experiments. The arc heater is supplied with air at 1 bar delivered by 1000-m^3 storage tank, which may be pressurized to 6×10^6 Pa. Mass flow rates up to 75 g/s can be controlled during the test time. The high enthalpy gas flows through a small settling chamber, then through a conical nozzle toward a vacuum chamber. The total nozzle, which is 0.40 m in length, has a throat diameter of 0.029 m, whereas the exit diameter and the nozzle half-angle are 0.20 m and 12 deg, respectively. The testing chamber has a cylindrical shape with a diameter of 2.6 m and a length of 2 m transversal to the flow direction. The test chamber is connected to the pumping system by a diffuser consisting of several cylindrical segments. The heat exchanger is installed downstream of the diffuser to cool down the heated gas to a temperature equivalent for the intake of the pumping system.

For the experiments, an arc current of 600 A is set with a mass flow rate of 0.049 $\mathrm{kg \cdot s^{-1}}$ and a stagnation pressure of 1.3×10^5 Pa. The temperature and the total enthalpy in the supply reservoir are estimated from the measured settling chamber pressure and the total mass flow rate and from calculation based on the equilibrium flow solution from the reservoir to the throat. The mass-averaged total enthalpy delivered to the gases is then 7.3 $\mathrm{MJ \cdot kg^{-1}}$, and the temperature is assumed to be equal to 3910 K. The stagnation conditions were controlled by means of a calibrated mass flow controller and a calibrated pressure transducer with a specified accuracy of 1% of the actual value. During the optical measurements, these parameters were held constant with a maximum deviation of 0.05 g/s for the mass flow rate and 1500 Pa for the stagnation pressure.

A water-cooled copper model is used for the experiment. It consists of a circular disk, 50 mm in diameter, with its axis along the center of the nozzle. The model is mounted on a holder, which can be moved in the range of 1000 mm transversal to the flow direction and 1500 mm along the flow direction.

B. Optical Setup

The core of the CARS system is an injection-seeded Q-switched Nd:YAG laser chain delivering 800 mJ of 1064-nm radiation in 17-ns-long pulses at a repetition rate of 10 Hz. The laser chain is composed of two laser heads (Quantel SF611) and a continuous wave diode-pumped seeder (Quantel YS700). The Nd:YAG rods are 7 mm in diameter and 9 mm in diameter for the oscillator and the amplifier, respectively. The 1064-nm output beam is frequency doubled in a KDP crystal providing 380 mJ at 532.1 nm with 14-ns pulses length and a spectral linewidth [full width at half maximum (FWHM)] less than 0.003 $\mathrm{cm^{-1}}$. The 1064-nm beam exiting from the first crystal is doubled again by another KDP crystal. Some additional 40 mJ at 532.1 nm are produced and used to pump a narrowband dye laser oscillator. Part of the 380 mJ main beam is used to pump the dye amplifier, and the remainder is used as the ω_1 pump beam. The resonator of the dye laser is composed of a 2100 grooves $\mathrm{mm^{-1}}$ holographic grating at grazing incidence, a flat rotating back mirror, and an intracavity prism beam expander yielding a linewidth (FWHM) of about 0.08 $\mathrm{cm^{-1}}$. The wavelength is selected by tilting the back mirror, which allows a coarse sweep from 500 to 800 nm in steps of 0.5 nm or a fine sweep of 6 nm around the coarse drive setting in fine steps of 0.01 nm. After the amplification, the ω_2 beam passes through a telescope to control the divergence and through appropriate optics for positioning the beam. The Stokes laser is tuned close to 607 nm and delivers 4 mJ in 11-ns pulses. At the output of the emitter bench, the ω_1 beam has already been split in two parallel beams separated 15 mm apart, and one of them is overlapped with the ω_2 beam (planar BOXCARS arrangement[9]). All beams are horizontally polarized.

A schematic of the CARS experimental configuration is presented in Fig. 1. The beams are focused first in the testing chamber with their axes perpendicular to the flow axis, where the ω_3 signal is created. Then, the CARS signal is split off, and the laser beams pass in a 1-atm pressure slow flow of argon, where they are refocused. A reference CARS signal is then created to monitor the fluctuations of direction and of pulse energy of the ω_1 and ω_2 beams. The reference and the sample CARS signals are filtered out from the pump

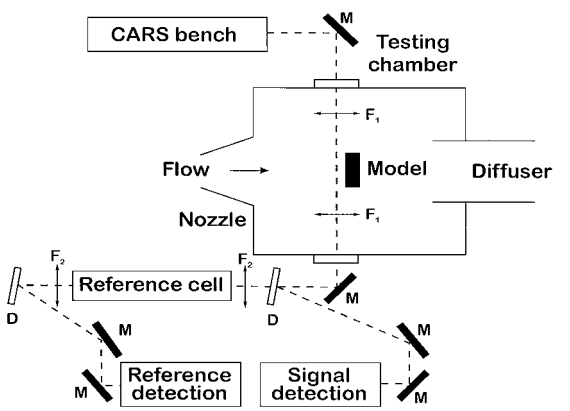

Fig. 1 Schematic of the CARS arrangement where F_1 and F_2 are achromats, M is the 400–700-nm broadband mirror, and D is the dichroic mirror.

beams using dichroic filters backed by double monochromators and transported to the photomultipliers using optical fibers. The single-pulse digitized sample and reference signals from gated electronics are recorded by the computer, which also drives the scanning of the dye laser frequency. The software calculates the signal-to-reference ratio and averages N laser shots at each laser position.

The focal lengths of the focusing optics inside the testing chamber are chosen according to the following conflicting constraints: first, short focal lengths are preferable to shorten the probe volume; second, long focal lengths are preferable to reduce the saturation effects that are likely to appear because powerful lasers are required to create the CARS signals in low-pressure media; third, the set of the focal lengths must be adapted to the dimensions of the facility. We know that 2×30 mJ of pump laser and 4 mJ of Stokes laser are the required energies to create measurable signals for the expected N_2 densities, and so the sample is selected to maintain[11]

$$0.1\Omega_s < \Delta\omega, \Delta\omega_d \tag{7}$$

$$0.1\Omega_R\tau < 1 \tag{8}$$

where Ω_s is the Stark frequency shift at pulse maximum, Ω_R the Rabi frequency, $\Delta\omega$ the free spectral range between the Stokes laser modes, $\Delta\omega_d$ the Doppler linewidth (FWHM), and τ the pulse duration. By the following of the development of Péalat et al.[11] and by assuming that $\Delta\omega \approx 0.01\ \text{cm}^{-1}$, $\Delta\omega_d \approx 0.016\ \text{cm}^{-1}$, and $\tau = 14$ ns, focal lengths longer than 700 mm verify the given constraints and cause negligible saturation effects.

The measurements are carried out at a position of 555 mm downstream from the nozzle exit and on the centerline region of the nozzle flow. The sample focal lengths are 750 mm. As a result, the achromats are installed inside the testing chamber. The sample probe volume (defined as the distance along which the entire anti-Stokes signal is created) is 25 mm long and 100 μm in diameter. The focal lengths of the focusing optics in the reference channel are 500 mm, according to the dimensions of the cell.

IV. Results

A. CARS Measurements

Figure 2 shows a sample nitrogen CARS spectrum recorded in the freestream. The experimental spectrum is recorded at 600 spectral positions with a frequency step of 0.01 cm^{-1} and a spectral resolution of 0.08 cm^{-1}. About 10 photoelectrons per pulse are detected at maximum. Consequently, a 30 laser shots average is taken at each spectral position to improve further the signal-to-noise ratio that results in a time of 40 mn to record a spectrum. As indicated in Fig. 2, the spectral bands detected by CARS are identified as the Q branches of the vibrational transitions (0, 1) and (1, 2). For each transition, clearly resolved are the rotational distributions of the two states of the molecule: the para-N_2 corresponding to the odd values of J and the ortho-N_2 corresponding to the even values of J. Rotational temperatures in each vibrational transition are measured by plotting the ortholines' and the paralines' intensities as a function of energy of

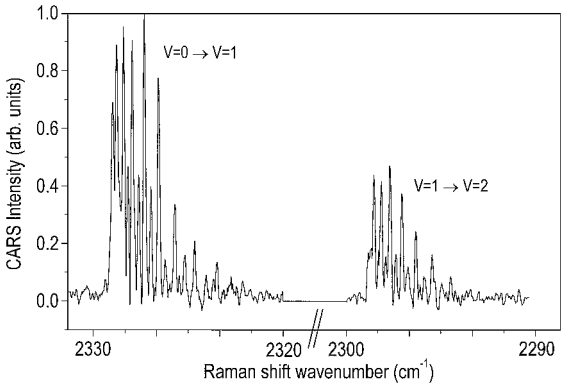

Fig. 2 Nitrogen CARS spectrum of the (0, 1) and (1, 2) vibrational transitions recorded in the freestream.

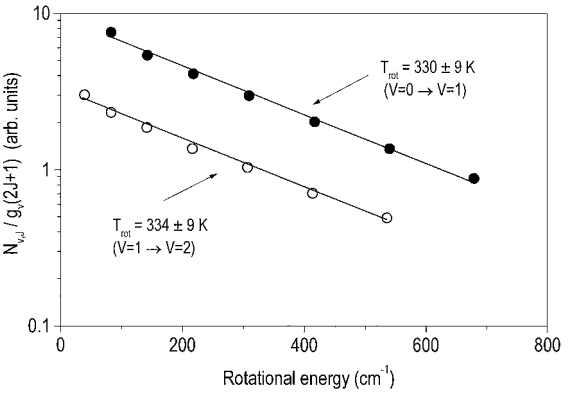

Fig. 3 Boltzmann plots of the orthorotational populations of the (0, 1) (●) and the (1, 2) (⊘) vibrational transitions recorded in the freestream.

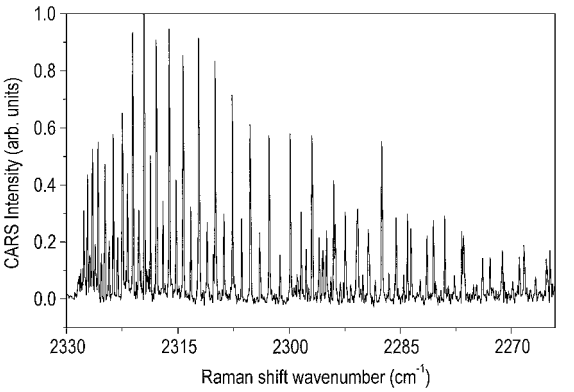

Fig. 4 Nitrogen CARS spectrum of the (0, 1) and the (1, 2) vibrational transitions recorded $x = 2$ mm from the model.

the rotational states. The log scale plot, as shown in Fig. 3, indicates that, within experimental errors, the rotational energy levels are in equilibrium. The rotational temperature is deduced from the slope of the linear best fit to the data. The scatter of the data points about the straight line, ±3%, merely reflects errors such as measurement uncertainty together with temporal fluctuations in mass flow rate, arc current, etc. The rotational temperatures, 330 and 334 K for the (0, 1) and (1, 2) transitions, respectively, are found nearly identical and demonstrate a nondependence of the rotational distributions vs v. The vibrational temperature, measured from the ratio between $v = 1$ and 0 populations is 2510 ± 130 K, where the accuracy reflects the 5% uncertainty on the vibrational populations. The experimental N_2 number density in the freestream is determined using the peak intensity of the different rotational lines compared with that of the static room temperature scan at known pressure (≈130 Pa). The resulting N_2 number density in the freestream is then found equal to 2.25×10^{15} molecule · cm^{-3} with an estimated uncertainty less than 10%.

To improve the data accuracy, average repetitive CARS measurements are performed during six runs at the same position in the freestream. As a result, a mean rotational temperature of 332 ± 6 K, a mean vibrational temperature of 2510 ± 80 K, and a mean N_2 number density of 2.2×10^{15} molecule · cm^{-3} with a standard deviation of 5% have been deduced giving indications about the reproducibility of the experiments and of the test conditions of the runs.

CARS measurements are then performed at several positions in the shock layer induced by the disk model. The spectra are recorded by moving the position of the model relative to a optical axis fixed at 555 mm from the nozzle exit. The displacement occurs only on the thickness of the shock layer (i.d. about 15 mm), which does not change the physical properties of the shock layer.

The shock wave is located at 12.5 mm upstream from the model. Far downstream from the bow shock (i.d. between 1 and 11 mm), the CARS spectra display the same profile for all of the explored positions. For instance, Fig. 4 shows a typical nitrogen CARS spectrum

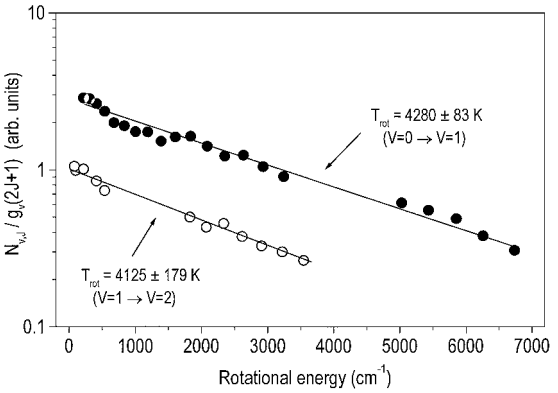

Fig. 5 Boltzmann plots of the orthorotational populations of the (0, 1) (●) and the (1, 2) (○) vibrational transitions recorded $x = 2$ mm from the model.

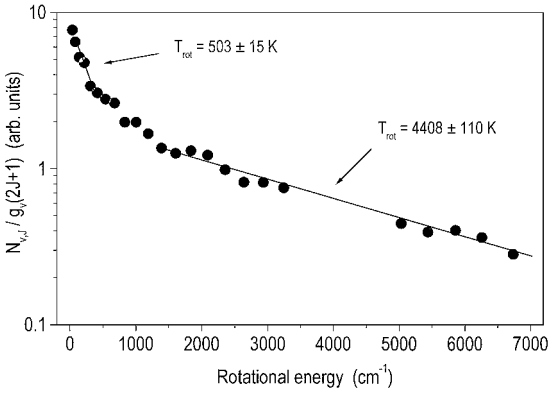

Fig. 6 Boltzmann plots of the orthorotational populations of the (0, 1) (●) vibrational transition $x = 12$ mm from the model.

recorded at 2 mm from the model. As was the case earlier, the intensity of the signal at the peak is about 10 photoelectrons per pulse. Consequently, The spectra are recorded at 1900 spectral positions. Each data point is the average of 30 laser shots, and the time needed to record a spectrum is about 2 h. The spectral bands measured are the (0, 1), the (1, 2) and the bandhead of the (2, 3) vibrational transitions, respectively, where rotational lines up to $J = 50$ are detected in each band.

Figure 5 shows the Boltzman diagrams of the orthostate for the (0, 1) and (1, 2) vibrational transitions. The two resulting distributions are in equilibrium, and the rotational temperatures associated to the (0, 1) and the (1, 2) transitions are found equal to 4280 ± 90 and 4125 ± 180 K, respectively. In the same manner, rotational temperatures deduced from the pararotational populations of each vibrational transition are identical. The vibrational temperatures for each state of N_2 are found similar (~2800 K) and less than the rotational temperatures. All of these results allow us to conclude that both N_2 states have the same enthalpy level and identical behaviors behind the shock wave.

In the shock-front region (i.d. between 12 and 13 mm), the rotational populations are no longer aligned. This is clearly observed on the Boltzmann diagram recorded at 12 mm from the model, shown in Fig. 6. One explanation to consider can be related to the dimensions of the probe volume and of the curvature of the shock wave. The dimensions of the probe volume, 25 mm long and 100 μm in diameter, seem to be longer. Mixing of gases coming from the freestream and from the shock layer, respectively, could be present in the probe volume. The resulting rotational distribution is, therefore, distorted, corresponding to the probing of adjacent N_2 samples with different thermodynamic conditions. The low-J rotational states will be characteristic of the nitrogen molecule close to the freestream whereas the high-J rotational populations will be representative of the nitrogen issued from the shock layer as seems to prove the data processing of the rotational distribution in Fig. 6. Although the rotational distribution is difficult to interpret

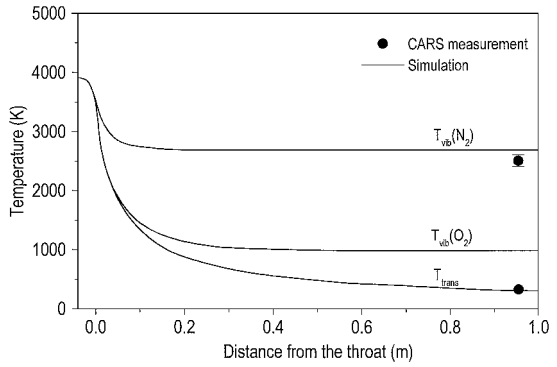

Fig. 7 Axial temperature distributions along the flow expansion.

to measure the temperature, information about the position of the shock wave can be easily determined as the boundary between positions displaying or not displaying a nonlinear rotational distribution for N_2.

B. Comparison Theory–Experiment

1. Nozzle Exit

The calculation of the flow in the nozzle has been performed using a quasi-one-dimensional approach. Seven orders of magnitude for the decrease of quadratic residuals have been obtained after 2000 iterations. In this calculation, the relaxation of N_2 and O_2 occurs through the vibrational–translational transfers with the molecules (O_2, N_2, and NO) and the atoms (O and N) of the gas mixture. Figure 7 shows the computational temperature distributions along the axis during the gas expansion. The freezing of the vibrational energy is brought into evidence by the different temperature distributions. The temperatures deduced from the experiments are also shown in Fig. 7. The calculated temperatures, $T = 305$ K and T_{vib} (N_2) = 2690 K, are in rather good agreement with the corresponding experimental values: $T_{rot} = 332 \pm 6$ K (assumed in equilibrium with the translational mode) and T_{vib} (N_2) = 2510 ± 80 K. The cause of the discrepancy between the theoretical and the experimental data could be explained by the possible effects of minor impurities species on the relaxation processes of N_2 (copper, water vapor, etc.). Among the species susceptible to be efficient, H_2O is known to catalyze the vibrational relaxation of numerous molecules. Its effect on the vibrational relaxation of N_2 ($v = 1$) is several orders of magnitude more efficient than that of the N_2 molecules alone. Recent calculations of the influence of H_2O on the vibrational relaxation processes of N_2 have showed noticeable differences on the temperature distributions.[23] For example, a mass fraction of H_2O as low as 0.005 is sufficient to carry away a decrease of the N_2 vibrational temperature and an elevation of the translational temperature similar to the experimental ones. An alternative explanation of the discrepancy may be that the vibrational temperature defined by the distribution of the low vibrational states could be substantially lower than the average (energy-averaged) vibrational temperature because of a possible so-called Treanor distribution due to a preferentially recombination in the higher energy states.[24,25]

The experimental total density of the flowfield is deduced from the N_2 number density and by assuming that the mole fractions of the gases are those predicted by the solver. The resulting total density in the freestream is then $1.40 \times 10^{-4} \pm 0.07 \times 10^{-4}$ kg/m^3, a value in fairly good agreement with the calculated total density equal to 1.6×10^{-4} kg/m^3.

2. Shock Layer

A bidimensional calculation has been performed around the model using a grid including 85 × 55 points (Fig. 8). The right angle of the model has been blunt with a small transition radius ($R = 2.5 \times 10^{-3}$ m) to avoid singularities during the computation. The calculation is performed using the freestream conditions calculated earlier as input conditions (Table 1). The wall is supposed noncatalytic, and its temperature is set at a constant value of $T_{wall} = 1300$ K, measured by a pyrometer during the experiment. Six orders of magnitude for the decrease of quadratic residuals have

Table 1 Input conditions for the shock layer simulation

Mach number and temperature, K	Density, kg/m^3
M = 7.8	ρ_∞ = 1.67E−04
T_{trans} = 305	ρ_{N2} = 1.24E−04
T_{vib} (N_2) = 2690	ρ_{O2} = 1.43E−05
T_{vib} (O_2) = 935	ρ_{NO} = 8.85E−06
	ρ_N = 3.76E−12
	ρ_O = 1.99E−05

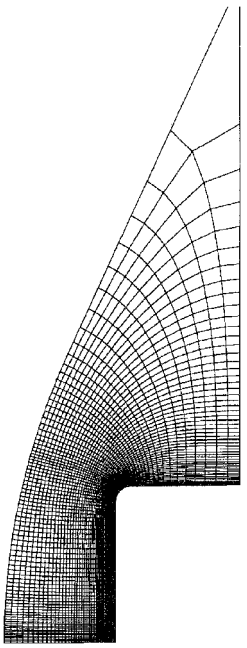

Fig. 8 Model computational grid (85 × 85).

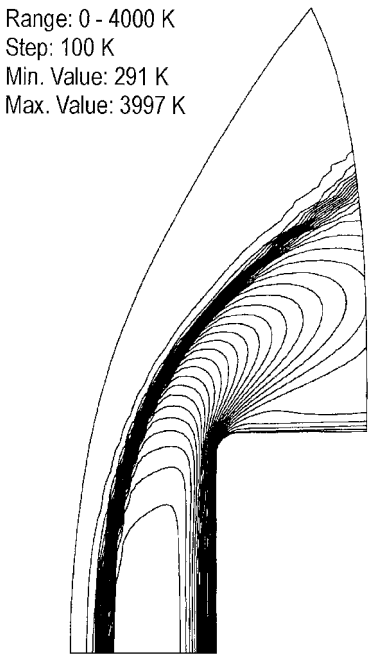

Fig. 9 Translational temperature isolines.

been obtained after 2000 iterations. The translational and N_2 vibrational temperature isolines are shown in Figs. 9 and 10, respectively, with the associated temperature ranges. Figure 11 shows the temperature distributions on the symmetry axis in the shock layer. The continuous and dotted lines display the calculated translational and N_2 vibrational temperatures, respectively. The calculation brings shows an important increase of translational temperature through the 1.5-mm-thick shock wave. The translational temperature displays a flat profile in a large portion of the shock layer before decreasing

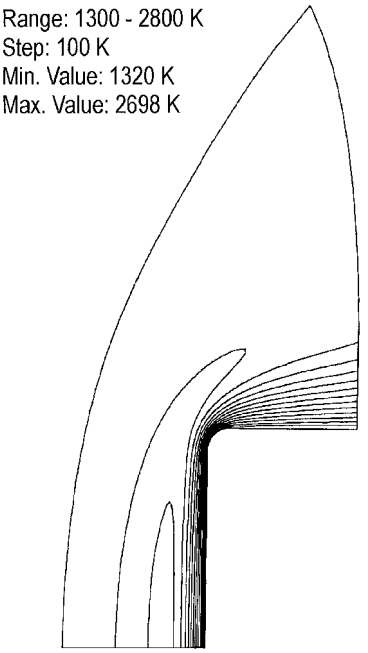

Fig. 10 Nitrogen vibrational temperature isolines.

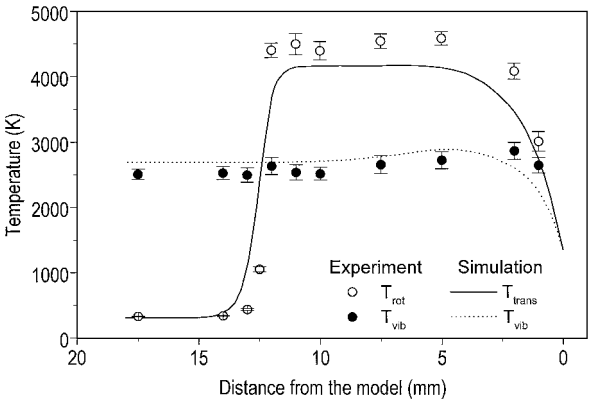

Fig. 11 Axial temperature distributions downstream from the bow shock.

strongly close to the wall. The vibrational temperature varies slowly in the shock layer from 2690 to about 2900 K. Near the wall, both temperatures become identical indicating a thermal equilibrium for the gases. The experimental data are also shown in Fig. 11. All of the rotational temperatures, measured by the analysis of the different rotational distributions of each state of the molecule, are displayed by the open symbols, whereas the filled symbols show the vibrational temperatures. The error bars represent the standard deviation of the measurements. As a first result, the bow shock is well captured at the same computational position. The observed reduction in the inferred thickness below the predicted value is a consequence of the difficulty to interpret accurately the observed rotational distributions. The experimental rotational temperature profile agrees fairly well with the numerical predictions, except in the postshock region, where the calculated temperatures are exceeded by 10%. The cause of this discrepancy is not yet known and is too large to be the result of systematic errors. One explanation could be an imprecise knowledge of the experimental temperature of the gases in the settling chamber. Circulation and mixing between the hot gas in the centerline region and the cold gas in the peripheral region could be present as suggested by Durgapal and Palmer.[26] Consequently, the experimental centerline enthalpy could be greater than the calculated mass-averaged total enthalpy, leading to an increase of the translational temperature in the shock layer. The measured vibrational temperature profile agrees with the predictions except close to the wall, where measured temperatures are higher. This increase could be due to a possible wall catalysis, which may lead

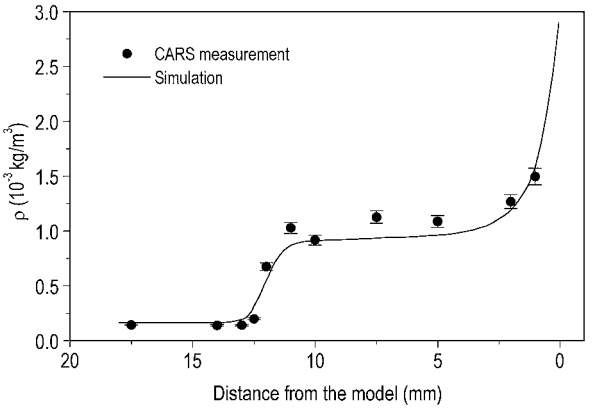

Fig. 12 Axial density distribution downstream from the bow shock.

to the formation of vibrationally excited molecules. More refined measurements closer to the wall are necessary to confirm this trend.

Figure 12 shows the comparison between experimental and computational density profiles in the shock layer. Whatever the position, differences by only 10% are noted, demonstrating a good agreement between the experiment and the calculation.

V. Conclusions

It has been demonstrated that scanning CARS allows rotational and vibrational temperatures and number density measurements in a continuous high enthalpy airflow, both in the freestream and behind to the shock layer induced by a model. Good agreement has been obtained with values predicted by the Navier–Stokes solver both in the freestream and behind the bow shock. As expected, vibrational nonequilibrium is demonstrated. The CARS method is proved to be a sensitive and useful probe of molecules under the high-temperature–low-density conditions obtained in a high enthalpy flow. The present work has, thus, highlighted the need for improved flowfield measurements over the usual conventional tools for CFD validation and has provided confidence in the CELHYO solver.

Acknowledgment

The authors would like to thank J. P. Taran from ONERA for the very helpful discussions and comments.

References

[1]Gillepsie, W. D., Bershader, D., Sharma, S. P., and Ruffin, S. M., "Raman Scattering Measurements of Vibrational and Rotational Distributions in Expanding Nitrogen," AIAA Paper 93-0274, 1993.

[2]Mohamed, A. K., Pot, T., and Chanetz, B., "Diagnostics by Electron Beam Fluorescence in Hypersonic," *16th International Congress on Instrumentation in Aerospace Simulation Facilities*, Institution of Electrical Engineers, July 1995.

[3]Beck, W. H., Koch, U., and Müller, M., "Spectroscopic Diagnostic Techniques for the High Enthalpy Shock Tunnel in Göttingen (HEG): Preparatory LIF Studies on Other Facilities," *Proceedings of the NATO Advanced Research Workshop on New Trends in Instrumentation for Hypersonic Research*, Vol. 224, Series E: Applied Sciences, Kluwer Academic Publishers, 1993, pp. 215–224.

[4]Pham-Van-Diep, G. C., Muntz, E. P., and Boyd, I. D., "Measurement of Rotational and Vibrational Population Distributions in a Hypersonic Flow of Chemically Reacting Iodine Vapor," AIAA Paper 93-2996, 1993.

[5]Arepalli, S., Yuen, E. H., and Scott, C. D., "Application of Laser Induced Fluorescence for Flow Diagnostics in Arc Jets," AIAA Paper 90-1763, June 1990.

[6]Koch, U., Gülhan, A., Esser, B., Grisch, F., and Bouchardy, P., "Rotational and Vibrational Temperature and Density Measurements by Planar Laser Induced NO-Fluorescence Spectroscopy in a Nonequilibrium High Enthalpy Flow," *RTO/AGARD Fluid Dynamics Panel Symposium, Advanced Aerodynamic Measurement Technology*, CP-601, AGARD, 1997, Paper 15.

[7]Massabiaux, B., Gousset, G., Lefebvre, M., and Péalat, M., "Determination of $N_2(X)$ Vibrational Level Populations and Rotational Temperatures Using CARS in a D. C. Low Pressure discharge," *J. Physique*, Vol. 48, Nov. 1987, pp. 1939–1949.

[8]Coquel, F., Flament, C., Joly, V., and Marmignon, C., "Viscous Nonequilibrium Flow Calculations," *Computing Hypersonic Flows*, Vol. 3, edited by J. J. Bertin, J. Périaux, J. Ballmann, Birkhäuser Boston, Cambridge, MA, 1993.

[9]Druet, S., and Taran, J. P., "CARS Spectroscopy," *Prog. Quant. Electr.*, Vol. 7, No. 1, 1981, pp. 1–72.

[10]Druet, S., Taran, J. P., and Borde, C., "Line Shape and Doppler Broadening in Resonant CARS and Related Nonlinear Processes Through a Diagrammatic Approach," *J. Physique*, Vol. 40, Sept. 1979, pp. 819–840.

[11]Péalat, M., Lefebvre, M., Taran, J. P., and Kelley, P. L., "Sensitivity of Quantitative Vibrational Coherent Anti-Stokes Raman Spectroscopy to Saturation and Stark Shifts," *Physical Review A: General Physics*, Vol. 38, No. 4, 1988, pp. 1948–1965.

[12]Lucht, R. P., and Farrow, R. L., "Saturation Effects in Coherent Anti-Stokes Raman Scattering Spectroscopy of Hydrogen," *Journal of the Optical Society of America B*, Vol. 6, 1989, pp. 2313–2325.

[13]Herzberg, G., *Molecular Spectra and Molecular Structure I: Diatomic Molecules*, Prentice–Hall, New York, 1939.

[14]Lambert, J. D., *Vibrational and Rotational Relaxation in Gases*, Clarendon Press, Oxford, 1977.

[15]Wray, K. L., "Shock Tube Study of the Vibrational Relaxation of Nitric Oxide," *Journal of Chemical Physics*, Vol. 36, 1962, pp. 2597–2603.

[16]Palmer, J. L., and Hanson, R. K., "PLIF Imaging in Free-jet Flows with Vibrational Nonequilibrium," AIAA Paper 93-0046, 1993.

[17]Gardiner, W. C., Jr., *Combustion Chemistry*, Springer-Verlag, Berlin, 1984.

[18]Landau, L., and Teller, E., "Theory of Sound Dispersion," *Physikalische Zeitschrift der Sowjetunion*, Vol. 10, 1936, pp. 34–43.

[19]Millikan, R. C., and White, D. R., "Systematics of Vibrational Relaxation," *Journal of Chemical Physics*, Vol. 31, 1959, pp. 3209–3213.

[20]Thivet, F., Perrin, M. Y., and Candel, S., "A Unified Nonequilibrium Model for Hypersonic Flows," *Physics of Fluid A*, Vol. 3, 1991, p. 2799.

[21]Coquel, F., Joly, V., and Marmignon, C., "Méthodes de décentrement hybrides pour la simulation d'écoulements en déséquilibre thermique et chimique," *Progress and Challenges in CFD Methods and Algorithms*, AGARD, 1995.

[22]Gülhan, A., Jörres, V., and Kindler, K., "Experiments on the Catalytic Efficiency of Heat Protection Materials in the Arc-Heated Facility Wind Tunnel (LBK) in Cologne," *Proceedings of the NATO Advanced Research Workshop on New Trends in Instrumentation for Hypersonic Research*, Vol. 224, Series E: Applied Sciences, Kluwer Academic Publishers, 1993, pp. 517–529.

[23]Joly, V., and Marmignon, C., "Effect of H_2O Vapor on the Vibrational Relaxation in Hypersonic Wind Tunnels," *Journal of Thermophysics and Heat Transfer*, Vol. 11, 1997, pp. 266–272.

[24]Treanor, C. E., and Marrone, P. V., "Effect of Dissociation on the Rate of Vibrational Relaxation," *Physics of Fluids*, Vol. 5, No. 9, 1962, pp. 1022–1026.

[25]Marrone, P. V., and Treanor, C. E., "Chemical Relaxation with Preferential Dissociation from Excited Vibrational Levels," *Physics of Fluids*, Vol. 6, No. 9, 1963, pp. 1215–1221.

[26]Durgapal, P., and Palmer, G., "Strongly Coupled Radiative Transfer and Joule Heating in the Cathode of an Arc Heater," AIAA Paper 93-2801, 1993.

R. P. Lucht
Associate Editor